---

**Article:**
Wang, L., Geddes, D.A., Walkley, B. orcid.org/0000-0003-1069-1362 et al. (3 more authors) (2020) The role of zinc in metakaolin-based geopolymers. Cement and Concrete Research, 136. 106194. ISSN 0008-8846

https://doi.org/10.1016/j.cemconres.2020.106194

---

# The Role of Zinc in Metakaolin-Based Geopolymers

Lei Wang[1,2,3], Daniel A. Geddes[1], Brant Walkley[1,4], John L. Provis[1], Viktor Mechtcherine[3], Daniel C.W. Tsang[2,*]

[1] Department of Materials Science and Engineering, The University of Sheffield, Sir Robert Hadfield Building, Mappin St, Sheffield S1 3JD, United Kingdom.

[2] Department of Civil and Environmental Engineering, The Hong Kong Polytechnic University, Hung Hom, Kowloon, Hong Kong, China.

[3] Institute of Construction Materials, Technische Universität Dresden, 01062 Dresden, Germany.

[4] Department of Chemical and Biological Engineering, The University of Sheffield, Sir Robert Hadfield Building, Mappin St, Sheffield S1 3JD, United Kingdom.

* Corresponding author: dan.tsang@polyu.edu.hk

## Abstract

Geopolymers are low-calcium, sustainable cementitious materials. The role of Zn, a known retardant used in Portland cement, in geopolymer systems is not well understood. This study scrutinises the effect of Zn on metakaolin-based geopolymer reaction mechanisms and kinetics, and investigates the incorporation mechanism of Zn in geopolymer gels. Isothermal calorimetry and X-ray diffraction analyses show that substitution of ZnO (20 mol.% c.f. metakaolin) significantly hinders reaction, likely due to preferential formation of a Na/K-Zn containing phase. Solid-state nuclear magnetic resonance spectroscopy shows that $Zn^{2+}$ partially substitutes for $Na^{+}/K^{+}$ in charge-balancing sites within the geopolymer gel. Setting time and leaching tests show that the retarding effect of Zn on reaction kinetics is significantly greater in Na-activated geopolymers compared with K-activated geopolymers, whereas Na-activated geopolymers exhibit superior fixation capacity to Zn. A lab-scale experiment

demonstrates that metakaolin-based geopolymers are promising candidates for the stabilisation/solidification of Zn-rich hazardous waste.

**Keywords:** geopolymer; alkali-activation; reaction kinetics; retarding mechanism; hazardous waste immobilisation.

**Highlights:**

- High-dosage of ZnO significantly hindered the geopolymer reaction process.
- Crystalline ZnO consumed in alkali-activation reaction to form new amorphous material.
- $Zn^{2+}$ partially replaced $Na^{+}/K^{+}$ in charge-balancing sites within geopolymer gel framework.
- Retarding effect of Zn on reaction kinetics was significantly greater in Na-activated geopolymers compared with K-activated geopolymers.
- Na-activated geopolymer performed with superior efficiency in Zn-immobilisation.

## 1. Introduction

Geopolymers are alternative cementitious materials comprised of a three-dimensionally cross-linked, highly polymerised, and non-crystalline alkali aluminosilicate network [1]. Geopolymers are produced via reaction of aluminosilicate precursors, such as metakaolin (MK), blast furnace slag, and pulverised fuel ash, with alkaline solutions, typically alkali silicate or alkali hydroxide [2]. Geopolymer cements offer up to 80% reduction of $CO_2$ emissions compared to Portland cement (PC) by avoidance of $CO_2$ release from limestone calcination and the need for high temperature (1400 °C) treatment during cement clinker production [3,4]. As a consequence, geopolymers are low-carbon, sustainable cementitious materials and viable substitutions for PC in certain applications. The nanostructure of geopolymer cements is different from that of PC, primarily due to the low-Ca content of

geopolymer systems [5]. Calcium silicate hydrate (C-S-H) gel is the main hydration product of PC and exhibits a tobermorite-like structure, whereas the sodium/potassium aluminosilicate hydrate ((N/K)-A-S-H) gel formed in geopolymer cements exhibits a fully polymerised and disordered structure [2]. When properly formulated, geopolymer cements exhibit superior performance to PC in many applications, including fire-resistant composites, acid-resistant concrete, and hazardous and radioactive waste immobilisation [6-9].

Cement-based stabilisation/solidification (S/S) is a widely accepted and reliable technology for soil remediation and hazardous waste treatment via chemical fixation and physical encapsulation of toxic or hazardous components [10-12]. Cementation of toxic or hazardous wastes offers advantages over other solidification approaches, such as low cost, ease of use, rapid waste processing, and high durability [13]. Furthermore, S/S products can be recycled and used as sustainable and value-added construction materials [14,15]. However, in PC-based S/S system, many toxic or hazardous elements can delay hydration and compromise the physicochemical properties of S/S products. Zinc (Zn) is particularly problematic, and is a well-known retarder in PC systems [16,17]. Previous research showed that the presence of 0.2 wt% ZnO in PC paste prolongs the initial and final setting times by 4 times and 3.5 times, respectively [18]. Zn in cement clinker should therefore be below a threshold of 0.7 wt%; higher content of Zn can significantly delay, and even halt, PC hydration [19,20]. Such adverse effects limit the application of PC for S/S of Zn-rich industrial waste [21]. The retarding mechanism has been attributed to the formation of $Ca(Zn(OH)_3)_2 \cdot 2H_2O$ which surrounds clinker particles [18], hindering the further dissolution and reaction, and depletes soluble calcium [22], limiting nucleation and growth of C-S-H gel or calcium aluminium silicate hydrate (C-A-S-H) gels. In both cases, the retarding mechanism results from the interaction of Ca and Zn in the cement system. Low-Ca or Ca-free geopolymer cements are have therefore

gained significant interest for S/S of Zn-contaminated waste.

Although there remains an absence in the literature of a complete mechanistic understanding of the interaction of Zn and geopolymer cement systems, recent findings [22] have shown that the presence of low-dosage ZnO of up to 1 wt% has a negligible inhibitory effect on the reaction process of low-Ca alkali-activated materials. Furthermore, MK-based geopolymers have the potential to adsorb Zn ions due to the porous and amorphous nature of MK [23], further reducing any inhibitory effect on reaction kinetics. However, many industrial processes produce Zn-rich by-products or wastes via different physicochemical processes (e.g. coagulation/precipitation and sedimentation). As a result, highly concentrated Zn is observed in mine tailings, smelter waste, and industrial sludge [24-26]. In particular, electroplating sludge contains approximately 46.6 wt% ZnO, and is therefore a severe threat to human health and to ecosystem. Therefore, to develop appropriate S/S technologies for the safe treatment of Zn-rich waste, the inhibitory effect of high amounts of Zn on the reaction mechanisms and kinetics in geopolymer systems must be investigated.

Ion retention, dictated by the incorporation mechanisms and mass transport processes, is the primary indicator of S/S efficiency when encapsulating toxic waste. Recent work has shown that the fully polymerised alkali aluminosilicate framework structure in geopolymer cements is beneficial for encapsulation of toxic elements within the structure [27], and that the negative charge due to Al(III) in fourfold coordination in (N,K)-A-S-H gels can be charge-balanced by alkaline earth cations $Ca^{2+}$ and $Sr^{2+}$ [28]. However, there remains an absence from the literature of a detailed understanding of the effect of high amounts of Zn on the reaction mechanisms and kinetics in the MK-based geopolymer cements.

To provide insight into the effect of Zn on the reaction mechanisms, kinetics and Zn-incorporation mechanisms of geopolymer cements, and to offer engineering solutions for the application of geopolymer-based S/S for Zn-rich waste, this study aims to: (i) elucidate the role of Zn in the reaction processes occurring during the formation of different (N,K)-A-S-H gels, including any inhibitory effects; (ii) assess the incorporation mechanisms of Zn in different geopolymer cement systems with varying alkalinity; (iii) evaluate the efficiency of geopolymer for S/S of Zn-rich sludge in terms of setting time, compressive strength, and leachability.

## 2. Materials and Methods

### *2.1 Materials*

In this study, MK was used as a precursor, and sodium or potassium silicate solutions were used as activators. High purity MK was purchased from BASF, Germany, with a $SiO_2/Al_2O_3$ ratio of 2.0 and a particle size $d_{50}$ of 25 μm. The activating solutions were made of either sodium or potassium silicate (PQ Silicates, UK) mixed with reagent grade MOH (M representing either Na or K; Fisher, UK). Zn-rich industrial sludge (46.6 wt% ZnO), used for geopolymer-based S/S, was collected from an electroplating factory in Zhejiang Province, China. The chemical composition and XRD patterns of this sludge are illustrated in Table S1 and Figure S1 (Supplementary Information), respectively. The dewatered sludge cake contained 57.2 wt% remaining water and yielded a 24.7 wt% loss on ignition. The sludge was freeze-dried and crushed into particles with diameters less than 0.3 mm before use. Additionally, high purity $ZnO/Zn(OH)_2$ was used to evaluate the role of Zn on the reaction mechanisms, kinetics and incorporation processes in geopolymer cements. $ZnO/Zn(OH)_2$ was synthesised from zinc nitrate hexahydrate (98% purity, Fisher) and sodium hydroxide (≥99% purity, Fisher) via a hydrothermal synthesis method, as described previously [29]. At atmospheric pressure and room temperature, almost all of the formed $\varepsilon$-$Zn(OH)_2$ was

126 transformed into ZnO. Thus, ZnO powder (≥95%) is a predominant component in the final
127 products, with trace amounts of $Zn(OH)_2$ [29]. The XRD pattern of the synthesised ZnO is
128 illustrated in Figure S1.
129
130 ***2.2 Sample Preparation***
131 Sodium silicate or potassium silicate were designed with a $SiO_2/M_2O$ molar ratio of 0.5, 1.0,
132 and 1.5, and a $H_2O/M_2O$ molar ratio of 13. In Zn-free geopolymer (control) system, $Al_2O_3/M_2O$
133 ratio was 1. In the Zn-substituted geopolymer system, $Al_2O_3/M_2O$ ratio was 0.8 and $ZnO/M_2O$
134 ratio was 0.2. For geopolymer samples with Zn-sludge addition, geopolymer paste/sludge
135 ratios were designed at 1:1, 1:2 and 1:4 by weight, and extra water (50% of dry sludge) was
136 added to achieve favourable flowability. The mixture design of geopolymer samples with and
137 without ZnO/Zn-rich sludge is illustrated in Table 1. For sample preparation, MK precursor
138 powder was mixed into the activating solution by a high-speed stirrer for 5 min. ZnO or sludge
139 powder was gradually added into the mixture and stirred for another 5 min. The fresh pastes
140 were transferred into sealed containers and steel moulds ($2 \times 2 \times 2$ $cm^3$). Sealed samples and
141 demoulded samples (after 3-day casting) were cured at 20 °C for 7 days and 28 days,
142 respectively. All the experiments on the cement pastes and sludge S/S blocks were performed
143 in triplicate and quadruple, respectively.
144

145 **Table 1.** Mixture design (molar ratios) of geopolymer samples with or without Zn.

| | $SiO_2/M_2O$ | $SiO_2$ | $Na_2O$ | $K_2O$ | $H_2O$ | MK | ZnO | Sludge* |
|---|---|---|---|---|---|---|---|---|
| **S/N 0.5** | 0.5 | 0.5 | 1 | 0 | 13 | 1 | 0 | 0 |
| **S/N 1.0** | 1.0 | 1 | 1 | 0 | 13 | 1 | 0 | 0 |
| **S/N 1.5** | 1.5 | 1.5 | 1 | 0 | 13 | 1 | 0 | 0 |
| **S/K 0.5** | 0.5 | 0.5 | 0 | 1 | 13 | 1 | 0 | 0 |
| **S/K 1.0** | 1.0 | 1 | 0 | 1 | 13 | 1 | 0 | 0 |
| **S/K 1.5** | 1.5 | 1.5 | 0 | 1 | 13 | 1 | 0 | 0 |
| **S/N 0.5-Z** | 0.5 | 0.5 | 1 | 0 | 13 | 0.8 | 0.2 | 0 |
| **S/N 1.0-Z** | 1.0 | 1 | 1 | 0 | 13 | 0.8 | 0.2 | 0 |
| **S/N 1.5-Z** | 1.5 | 1.5 | 1 | 0 | 13 | 0.8 | 0.2 | 0 |
| **S/K 0.5-Z** | 0.5 | 0.5 | 0 | 1 | 13 | 0.8 | 0.2 | 0 |
| **S/K 1.0-Z** | 1.0 | 1 | 0 | 1 | 13 | 0.8 | 0.2 | 0 |
| **S/K 1.5-Z** | 1.5 | 1.5 | 0 | 1 | 13 | 0.8 | 0.2 | 0 |
| **N-S1** | 1.0 | 1 | 1 | 0 | 13 | 1 | 0 | 1:1 |
| **N-S2** | 1.0 | 1 | 1 | 0 | 13 | 1 | 0 | 1:2 |
| **N-S4** | 1.0 | 1 | 1 | 0 | 13 | 1 | 0 | 1:4 |
| **K-S1** | 1.0 | 1 | 0 | 1 | 13 | 1 | 0 | 1:1 |
| **K-S2** | 1.0 | 1 | 0 | 1 | 13 | 1 | 0 | 1:2 |
| **K-S4** | 1.0 | 1 | 0 | 1 | 13 | 1 | 0 | 1:4 |

146 $M_2O$: $Na_2O$ or $K_2O$; MK: metakaolin

147 *binder-to-sludge mass ratio

148

149 ***2.3 Characterisation and Analyses***

150 The initial and final setting times of the geopolymer samples with or without ZnO/sludge were
151 examined by a Vicat apparatus [30]. The uniaxial compressive strength of the sludge-based
152 blocks was tested using a universal testing machine at a loading rate of 0.3 MPa $s^{-1}$ [31]. The
153 kinetics of the reaction of Zn-incorporated geopolymer samples were assessed using an
154 isothermal calorimeter (TAM Air instrument) at 20 ± 0.02 °C. The leachability of Zn/sludge-
155 incorporated samples was tested according to the Toxicity Characteristic Leaching Procedure
156 (TCLP) [32]. The leaching concentrations of toxic elements were detected by means of
157 inductively coupled plasma atomic emission spectrometry (ICP-AES, Spectro Arcos).

158

159 Chemical components of the geopolymer samples were analysed by thermogravimetric

160 analysis coupled with mass spectrometry (TGA-MS, Perkin Elmer TGA 4000 coupled to MS)
161 at a heating rate of 10 °C $min^{-1}$ from 30 °C to 1000 °C with nitrogen as the purging gas. All
162 samples were held at 30 °C for 20 min before the heating process. Water vapour, carbon
163 monoxide, nitrogen, oxygen, and carbon dioxide were analysed during the programmed heating
164 process. The surface morphology of the geopolymer samples was observed using by scanning
165 electron microscopy (SEM) with energy-dispersive X-ray (EDX) (QUANTA FEG 250).
166 Elemental mapping was performed on the crushed samples. Back scattered electron (BSE)
167 imaging was conducted on the polished geopolymer samples. The mineralogy of the powdered
168 samples was scanned using X-ray diffraction (XRD) (Bruker D8) in the range 2θ of 5-70° and
169 at a step size of 0.020°. A Cu anode was used as source and the Cu K-α wavelength was 1.5406
170 Å. A 10 wt% MgO was incorporated as an internal standard to quantify the content of ZnO
171 engaging in reaction.
172
173 The local structure of geopolymer reaction products was evaluated using solid-state magic
174 angle spinning (MAS) nuclear magnetic resonance (NMR) spectroscopy. The $^{29}Si$ and $^{27}Al$
175 spectra were acquired using a 500 MHz ($B_0$ = 11.7 T) solid-state NMR spectrometer
176 (GEOL500), yielding a Larmor frequency of 99.362 MHz for $^{29}Si$ NMR and 130.318 for $^{27}Al$.
177 The chemical shifts of $^{29}Si$ and $^{27}Al$ were referenced to external standards of tetramethylsilane
178 (TMS) and a 1.0 M aqueous solution of $AlCl_3 \cdot 6H_2O$, respectively. The $^{29}Si$ experiments were
179 conducted using a 7 mm standard bore, one pulse MAS probe head, a rotational rate of $\nu_R$ =
180 4.5 kHz, and a recycle delay of 30 s, acquiring from 108 to 2,000 scans. $^{27}Al$ NMR experiments
181 were conducted using a 4 mm MAS probe, a rotational rate of $\nu_R$ = 10 kHz, a recycle delay of
182 2 s with 1000 scans. Gaussian peak profiles were used for the fitting of $^{29}Si$ MAS NMR spectra.
183 A single Gaussian peak was used for representing different $Q^n$(mAl) species, and these peaks
184 were used to create a simulation of the $^{29}Si$ NMR spectra by using a least-squares fitting

method. Peak intensities are consistent with the structural constraints described by the statistical thermodynamic model for (N,K)-A-S-H products [33]. The molar ratio of Si/Al in (N,K)-A-S-H gel can be calculated based on Engelhardt's formula [34] (Eq. 1):

$$\frac{\mathrm{Si}}{Al} = \frac{\sum_{m=1}^{4} I_{AQ^4}(mAl)}{\sum_{m=1}^{4} 0.25 \times m \times I_{AQ^4}(mAl)} \quad (1)$$

Where $I_{AQ}{}^4$(mAl) is the normalised relative integral areas of $^{29}$Si MAS NMR fitting peaks of each $Q^4$(mAl) site in the geopolymer gel.

## 3. Results and Discussion

### *3.1 The Role of Zn in the Alkali-Activation Reaction*

Figure 1 illustrates the heat evolution curves for the geopolymer pastes with and without ZnO. As shown in Figure 1c, Na-activated geopolymer (S/N 1.0) samples presented a short dormant period and the time to reach the reaction peak (TTRP) was 6.4 h. By comparison, the TTRP of K-activated geopolymer (S/K 1.0) samples was longer. This indicated that the reaction in Na-based geopolymer was relatively vigorous in the early stage. However, the cumulative heat from S/K 1.0 surpassed S/N 1.0 samples after 37.8 h (Figure 1a). After substitution of ZnO, the TTRPs were significantly prolonged and the cumulative heat was reduced. Interestingly, TTRP in S/N 1.0-Z (39.3 h) was longer than that in S/K 1.0-Z samples (28.6 h), and cumulative heat in S/N 1.0-Z samples was relatively low during the reaction over 120 h, which reflected that Zn interacted with geopolymer chemically and had a more significant delay effect on the Na-activated geopolymer.

From Figure 1b & d, in low-alkali geopolymer samples, i.e., $SiO_2/M_2O$ molar ratio of 1.5, the TTRPs were longer and cumulative heats were lower than the values for high-alkali geopolymer samples ($SiO_2/M_2O$ ratio of 1.0). This is ascribed to low concentrations of sodium and potassium ions limiting nucleation and growth of the (N,K)-A-S-H gel [22]. It should be

noted that TTRPs in S/M 1.5-Z samples were much longer than that in S/M 1.0-Z samples. This revealed that while Zn exerted an inhibitory effect on both high- and low-alkali geopolymers, the effect was most pronounced in low-alkali geopolymers. The associated variations in setting time are discussed in Section 3.3.

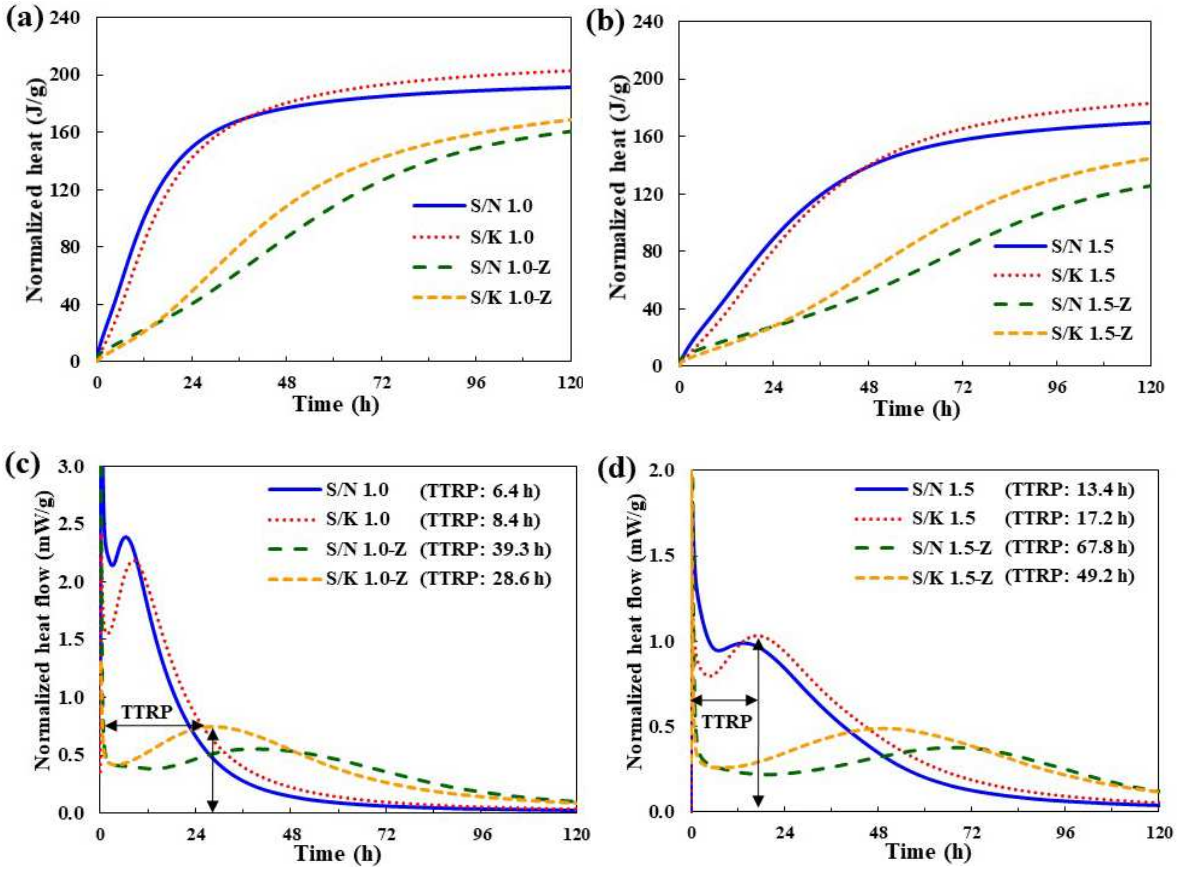


**Figure 1.** Isothermal calorimetry data of geopolymer pastes with and without ZnO: (a) cumulative heat of geopolymer pastes with $SiO_2/M_2O$ ratio of 1.0; (b) cumulative heat of geopolymer pastes with $SiO_2/M_2O$ ratio of 1.5; (c) heat flow corresponding to (a); (d) heat flow corresponding to (b). (TTRP: time to reach the reaction peak).

Based on simulation results obtained using Visual MINTEQ software (Table S2), $Zn(OH)_3^-$ was the dominant dissolved species (13.3% to 80.5%) of Zn in S/N 1.0-Z samples at high alkaline levels (pH 13-14), although the solubility of ZnO was minimal (less than 0.355%). Similarly, the $Zn(OH)_3^-$ was also the dominant dissolved species in the S/K 1.0-Z samples. Previous studies [22,35] reported that the existence of a metastable Ca-Zn phase

227 ($Ca(Zn(OH)_3)_2 \cdot 2H_2O$) in the Zn-incorporated cement system poisoned the nucleation and
228 growth of C-S-H gel. Considering geopolymer systems contain high concentrations of $OH^-$,
229 $Na^+$ and $Zn(OH)_3^-$ (Table S2), there is a possibility that a Na/K-Zn phase (e.g.,
230 $(Na/K)(Zn(OH_3)_2) \cdot nH_2O$) was generated in Zn-incorporated geopolymer systems. Therefore,
231 the ZnO retarding mechanism in geopolymer could be attributed to the preferential formation
232 of such a Na/K-Zn phase that may inhibit the nucleation and growth of (N,K)-A-S-H gel.
233
234 ***3.2 Efficacy of Zn on Reaction Products of Geopolymer***
235 TGA curves of 28-d cured geopolymer samples are shown in Figure 2. A remarkable mass loss
236 peak existed from 30 °C to 300 °C in the S/N 1.0 samples, which was associated with $H_2O$
237 release, as detected by MS analysis (Figure 2b). The water release resulted from the evaporation
238 of free water, physically adsorbed water, and chemically bound water from the geopolymer
239 gels [36,37]. The K-activated samples (S/K 1.0) showed similar mass loss peaks in the same
240 range. However, the total mass loss (18.0%) was smaller than the value in the S/N 1.0 samples
241 (22.4%) (Figure 2a). This phenomenon was in line with previous experimental findings [38,39],
242 where greater geopolymerisation with a Na-based activator led to a larger mass loss for Na-
243 based geopolymer. Herein, other potential reasons come to light. Because the ionic radius of K
244 (152 pm) is larger than that of Na (116 pm), the N-A-S-H gel with relatively small molar
245 volume may adsorb more water compared to K-A-S-H gel. Assuming per-unit of N-A-S-H-
246 and K-A-S-H-gel containing the same molar weight of bound water, due to the relatively large
247 molar mass of K, the mass fraction of $H_2O$ in K-based systems is relatively low, resulting in
248 the lower mass loss.

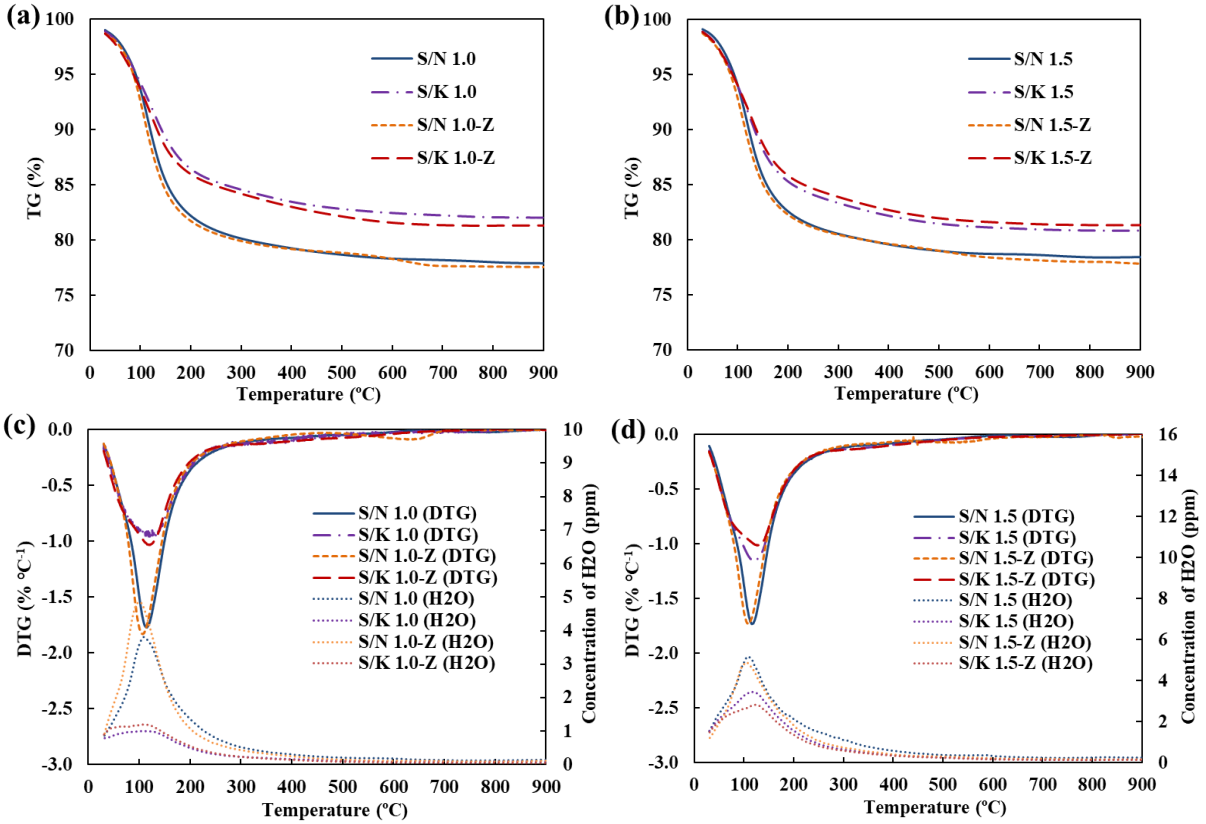


**Figure 2.** TGA of 28-d cured geopolymer pastes with and without ZnO: (a) TG curves of samples with $SiO_2/M_2O$ molar ratio of 1.0; (b) TG curves of samples with $SiO_2/M_2O$ molar ratio of 1.5; (c) DTG and water release curves corresponding to (a); (d) DTG and water release curves corresponding to (b). Water release curves in c) and d) were obtained from mass spectrometry data.

From Figure 2a & c, the partial substitution of ZnO had a negligible effect on mass loss or water release of Na/K-based geopolymer samples. Here it should be noted that the decomposition temperature of $Zn(OH)_2$ (125 °C) lies in the range of 30 °C to 300 °C [40,41]. Thus, based on TGA results, it is difficult to determine the contents of geopolymer gels and zinc hydroxide in S/N 1.0-Z and S/K 1.0-Z samples. As shown in Figure 2b, low-alkali geopolymer samples with an S/M ratio of 1.5 showed a relatively low mass loss, suggesting a small amount of reaction products in low-alkali samples. In the low alkali geopolymer system, incorporating ZnO also had a negligible effect on the variability of mass loss according to the TGA data.

XRD analysis was used to investigate the reaction products of geopolymer samples both with and without ZnO substitution. From Figure S1, there is a predominant, broad peak due to diffuse scattering centred at approximately 22° in the raw metakaolin curve, consistent with the amorphous nature of MK. Sharp peaks at 25.3° and 32.6° are attributed to a small amount of anatase ($TiO_2$). After a 7-d reaction at 20 °C (Figure 3a), two broad peaks centred at 11° and 29° appeared in the MK-based geopolymer samples, indicating the formation of crystallographically disordered products [28]. Na-activated samples and K-activated samples showed similar XRD patterns. MgO (analytical reagent) was added to the samples prior to XRD analysis as an internal standard to quantify the degree of ZnO involved in the reaction. However, after 7-d curing, the major ZnO peaks at 31.8°, 34.4°, and 36.3° had completely disappeared in the S/N 1.0-Z and S/K 1.0-Z samples, while other crystalline peaks of $TiO_2$ and MgO still existed. This demonstrated that all the ZnO (observable by XRD) had reacted and formed amorphous components. In alkaline solution, zinc and silicate ions can form amorphous zincate-silicate complexes [42], e.g., $[(HO)_3ZnO(SiO_2)O(SiO_2)OH]^{6-}$ and $[(HO)_3ZnOSiO_2OH]^{4-}$. In this study, the inclusion of ZnO in the reaction mixture did not change the line-shape of the XRD patterns of the geopolymer binders, suggesting that ZnO did not alter the general structure of major reaction products.

The XRD patterns of low-alkali geopolymer samples (S/M of 1.5) were very similar to those of S/M 1.0 geopolymer samples (Figure 3a). Similar to observations for the high-alkali geopolymers, the substitution of ZnO in the low-alkali system did not change the lineshape of the XRD patterns. After 28-d curing, the ZnO peak disappeared, and no new peak appeared in both the S/M 1.0-Z and S/M 1.5-Z geopolymer systems (Figure 3b). Therefore, the XRD results indicated that ZnO reacted during alkali-activation to formed amorphous products; however, ZnO did not change the general structure of the major reaction products.

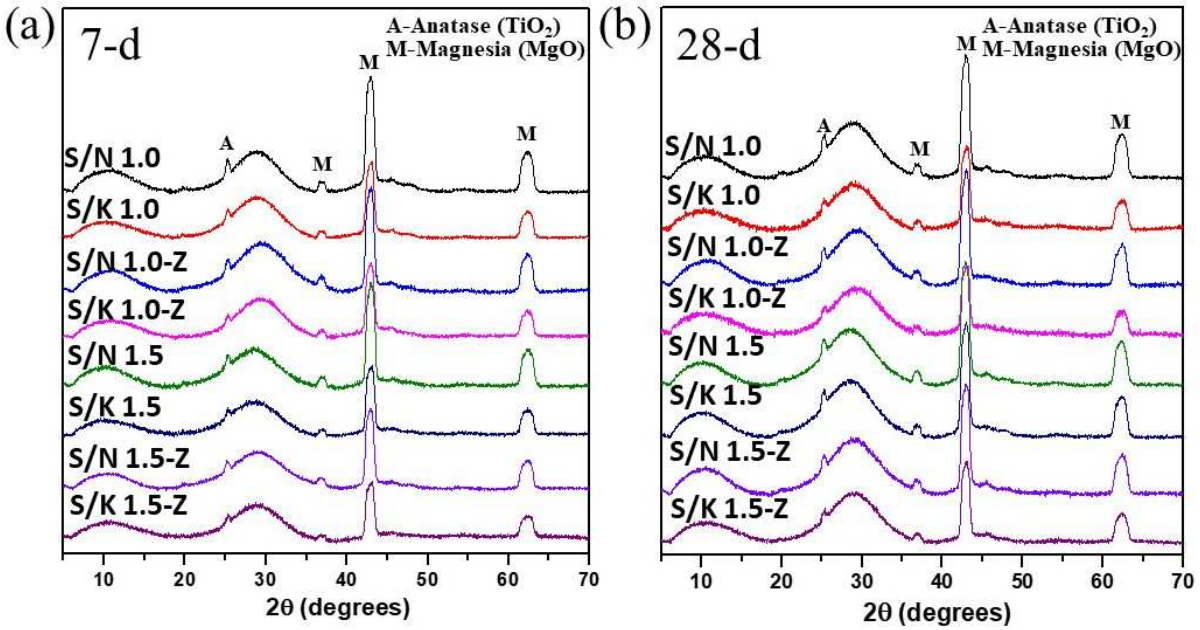


**Figure 3.** XRD data of geopolymer pastes with or without ZnO: (a) 7-d cured geopolymer pastes; (b) 28-d cured geopolymer pastes.

As illustrated in Figure S2a, the $^{29}$Si MAS NMR spectra of MK showed a broad resonance arising from a distribution of isotropic chemical shifts, $\delta_{iso}$, from -80 to -125 ppm, with the highest intensity at $\delta_{iso}$ = -108 ppm. This suggests a wide distribution of silicon environments and a significant degree of disorder, consistent with the broad amorphous peak in XRD patterns and previous work in the literature [44]. Spectral fitting indicated that the resonances were attributed to $Q^4$(0Al), $Q^4$(1Al), $Q^4$(2Al), $Q^4$(3Al) and $Q^4$(4Al). Among them, $Q^4$(0Al) and $Q^4$(1Al) represented approximately 46% and 24%, respectively. It is noted that the large proportion of $Q^4$(0Al) was probably due to over-calcination of kaolinite, which may influence the geopolymerisation. The detailed parameters of fitting peaks in raw MK are shown in Table S3, and the full spectra of MK and geopolymers are illustrated in Figure S3. After 28-d curing, data for S/N 1.0 and S/K 1.0 samples exhibited a resonance from $\delta_{iso}$ = -75 to -115 ppm (Figure 4a & b), with the highest intensity at $\delta_{iso}$ = -89.5 ppm and -90.5 ppm, respectively (Table S3). This suggests that the geopolymer gels were dominated by resonances of fully polymerised $Q^4$

species with high Al substitution, i.e., $Q^4$(4Al) and $Q^4$(3Al). The fitting and quantification results from Figure 4 and Table 2 illustrate that the N-A-S-H gel in the S/N 1.0 samples was composed of approximately 32% $Q^4$(4Al), 43% $Q^4$(3Al), 19% $Q^4$(2Al), 4% $Q^4$(2Al) and 2% $Q^4$(2Al), with a Si/Al molar ratio of 1.34. The detailed parameters of fitting peaks in geopolymers are shown in Table S3. K-A-S-H gel in S/K 1.0 samples had similar distributions of $Q^4$(mAl) sites and the Si/Al molar ratio was 1.40. The Si/Al molar ratio was lower than the value in the initial mixture, suggesting the preferential formation of Al-rich geopolymer gel. After substitution of ZnO, the $Q^4$(4Al) content was much larger than $Q^4$(3Al) content in S/N 1.0-Z sample, and consequently it had a relatively low Si/Al molar ratio (1.21) (Table 2). This is possibly due to the divalent charge $Zn^{2+}$ cation substituting the monovalent charge $Na^+$ cation, leading to an increase of charge-balancing capacity [28] (schematically illustrated in Figure 5).

By comparison, the substitution of ZnO only slightly decreased $Q^4$(3Al) content and increased $Q^4$(4Al) content in K-activated system (Figure 4d). The magnitude of the reduction of Si/Al molar ratio in K-activated system was relatively small compared to that of Na-activated system. This discrepancy can be attributed to differences of ionic radii between $Na^+$ and $K^+$. The ionic radius of $Zn^{2+}$ (88 pm) is closer to the radius of $Na^+$ (116 pm), compared to the value of $K^+$ (152 pm) [43]. Thus, $Zn^{2+}$ can more easily substitute for $Na^+$ cation than $K^+$ cations. This difference in Zn incorporation is likely to result in differences in Zn leachability in Zn-incorporated samples (discussed in Section 3.3).

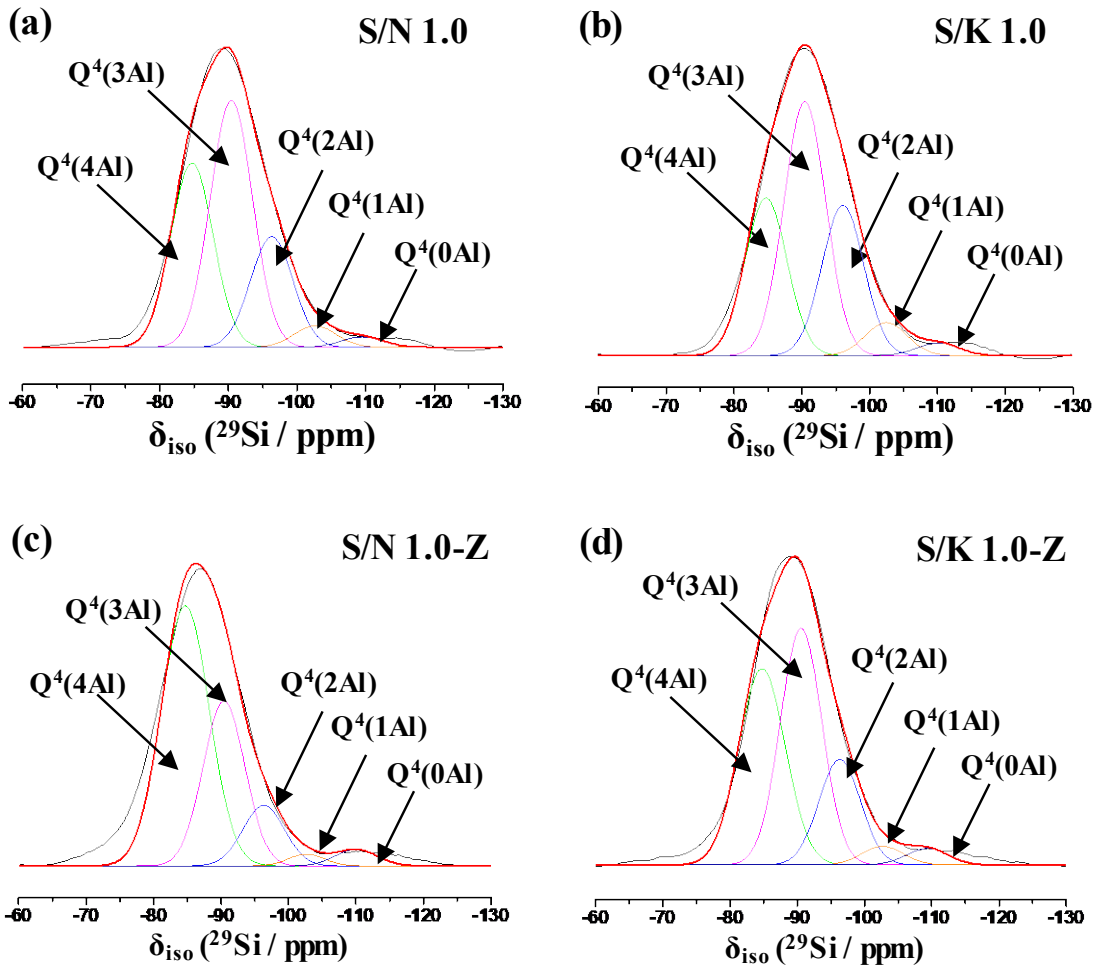


**Figure 4.** $^{29}$Si MAS NMR spectra ($B_0$ = 11.7 T, $\nu_R$ = 4.5 kHz) and associated fitting peaks for 28-d cured geopolymer pastes: (a) Na-activated geopolymer; (b) K-activated geopolymer; (c) Na-activated geopolymer with ZnO; (d) K-activated geopolymer with ZnO.

**Table 2.** Relative integral areas for $Q^4$(mAl) sites within (N,K)-A-S-H gel.

| | Relative integral area (%)* | | | | | |
|---|---|---|---|---|---|---|
| | $Q^4$(4Al) | $Q^4$(3Al) | $Q^4$(2Al) | $Q^4$(1Al) | $Q^4$(0Al) | Si/Al |
| S/N 1.0 | 32 | 43 | 19 | 4 | 2 | 1.34 |
| S/K 1.0 | 26 | 42 | 25 | 5 | 2 | 1.40 |
| S/N 1.0-Z | 54 | 30 | 11 | 2 | 3 | 1.21 |
| S/K 1.0-Z | 37 | 40 | 18 | 3 | 3 | 1.30 |

* The relative integrated intensity is obtained by simulating the $^{29}$Si MAS NMR spectra and is normalised to the sum of all sites in geopolymers. Error in the relative integral area is approximately 1%.

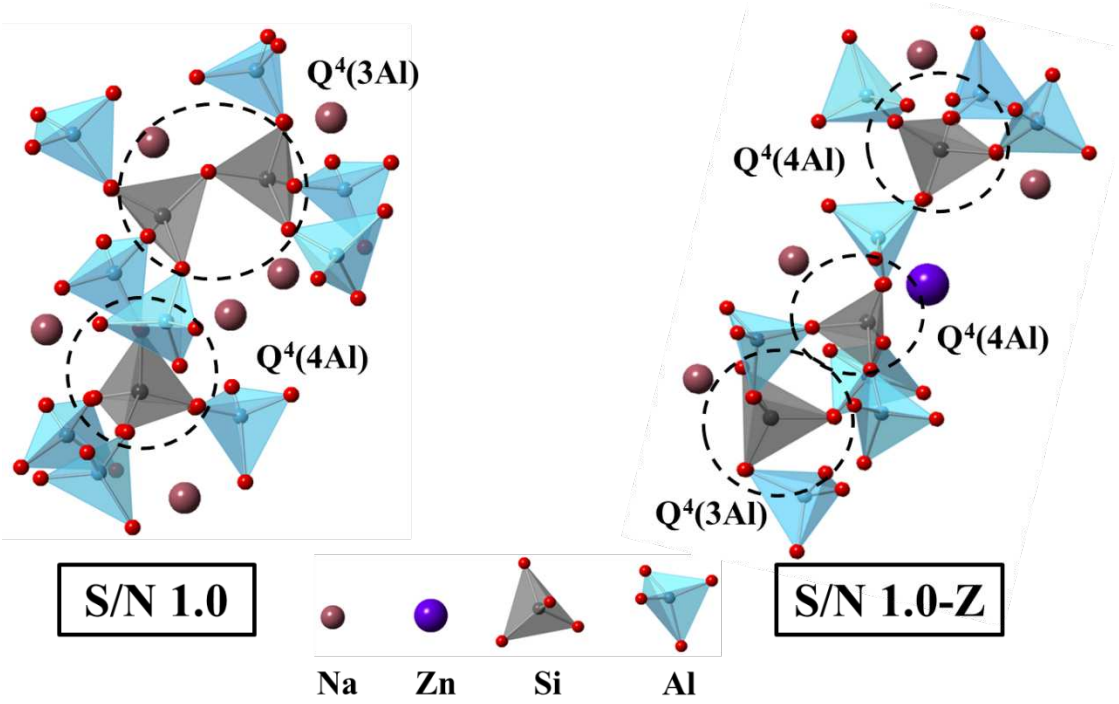


**Figure 5.** Schematic illustration of Na/Zn-A-S-H gels in S/N 1.0 and S/N 1.0-Z samples.

The $^{27}$Al MAS NMR spectrum of MK (Figure S2) shows three broad resonances at $\delta_{iso}$ = 60 ppm, 27 ppm, and -2 ppm, respectively, due to Al in tetrahedral, pentahedral, and octahedral coordination [44]. After 28-d curing, the data for geopolymer samples exhibited a high intensity resonance due to tetrahedral Al at $\delta_{obs}$ = 56 ppm (Figure 6). This signified that most Al in metakaolin took part in the reaction, consistent with observations from the $^{29}$Si MAS NMR and XRD data. The resonance at $\delta_{obs}$ = 56 ppm is ascribed to tetrahedral Al in a fully polymerised tetrahedral site ($q^4$) resulting from the substitution of $Al^{3+}$ for $Si^{4+}$ in the (N,K)-A-S-H framework [45], with the resultant negative charge balanced by alkali cations [46]. The incorporation of ZnO shifted the tetrahedral Al resonance to slightly higher $\delta_{obs}$ values, e.g., 0.37 ppm increment in the Na-activated samples, and 0.18 ppm increment in the K-activated samples. Such slight shifts may result from the partial substitution of $Zn^{2+}$ for $Na^+$ and $K^+$ in charge balancing sites in the (N,K)-A-S-H gel. $Zn^{2+}$ substitution had a negligible influence on the lineshape of the $^{27}$Al MAS NMR spectra, indicating that it did not significantly change the nanostructure of the geopolymer gels, which is consistent with XRD results. It is noted that

357 $^{23}$Na MAS NMR and $^{39}$K MAS NMR may provide useful information about the (Na,Zn)-A-S-
358 H gel, Na-Z phase, (K,Zn)-A-S-H gel, and K-Z phase, which would be required for further
359 quantifying the structural change of products in future studies.
360

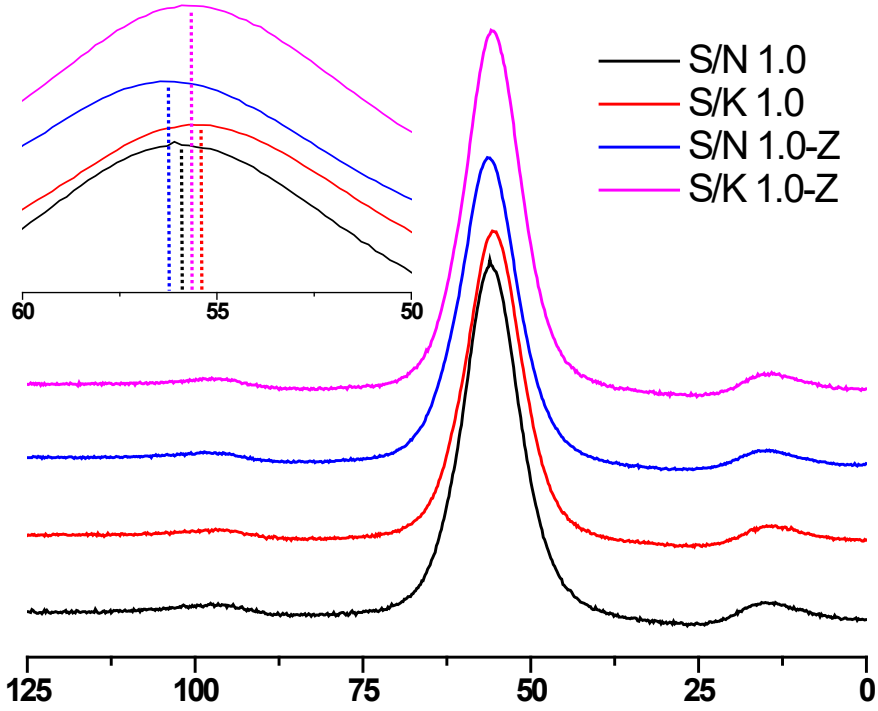


361
362 **Figure 6.** $^{27}$Al MAS NMR spectra ($B_0$ = 11.7 T, $\nu_R$ = 10.0 kHz) for 28-d cured geopolymer
363 pastes.
364
365 SEM image (Figure 7a) reveals some voids and microcracks on the fracture surface of S/N 1.0
366 samples, possibly due to the entrainment of air bubbles during the rapid geopolymerisation
367 when Na is the alkali source. By comparison and as shown in Figure 7b, S/K 1.0 samples
368 exhibited dense and flat surfaces with few voids, which is attributed to less rapid reaction
369 kinetics as revealed by isothermal calorimetry results. After ZnO substitution, many
370 agglomerates were observed on the matrix in S/N 1.0-Z samples (Figure 7c). Elemental
371 mapping (Figure 7e) verified that the porous blocks were composed of O, Al and Si, which
372 possibly resulted from the unreacted MK. Moreover, Zn was homogeneously distributed on

matrix. Theoretically, some zincate-silicate complexes can form in an alkaline solution [42]; however, the specific nature of the agglomerates in S/N 1.0 samples requires further investigation. By comparison, there were no observable agglomerates in S/K 1.0-Z samples, although the ZnO incorporation caused more voids (Figure 7d). The elemental mapping in Figure 7f also indicated that Zn was homogeneously distributed in the geopolymer matrix in the S/K 1.0-Z samples. The BSE images showed that the microstructure of S/N 1.0-Z samples was much denser than that of S/K 1.0-Z samples (Figure S4). The different microstructures observed in samples may influence the physicochemical properties of the geopolymer cements. Therefore, the effects of Zn on setting time and ion retention of the geopolymer cements were investigated.

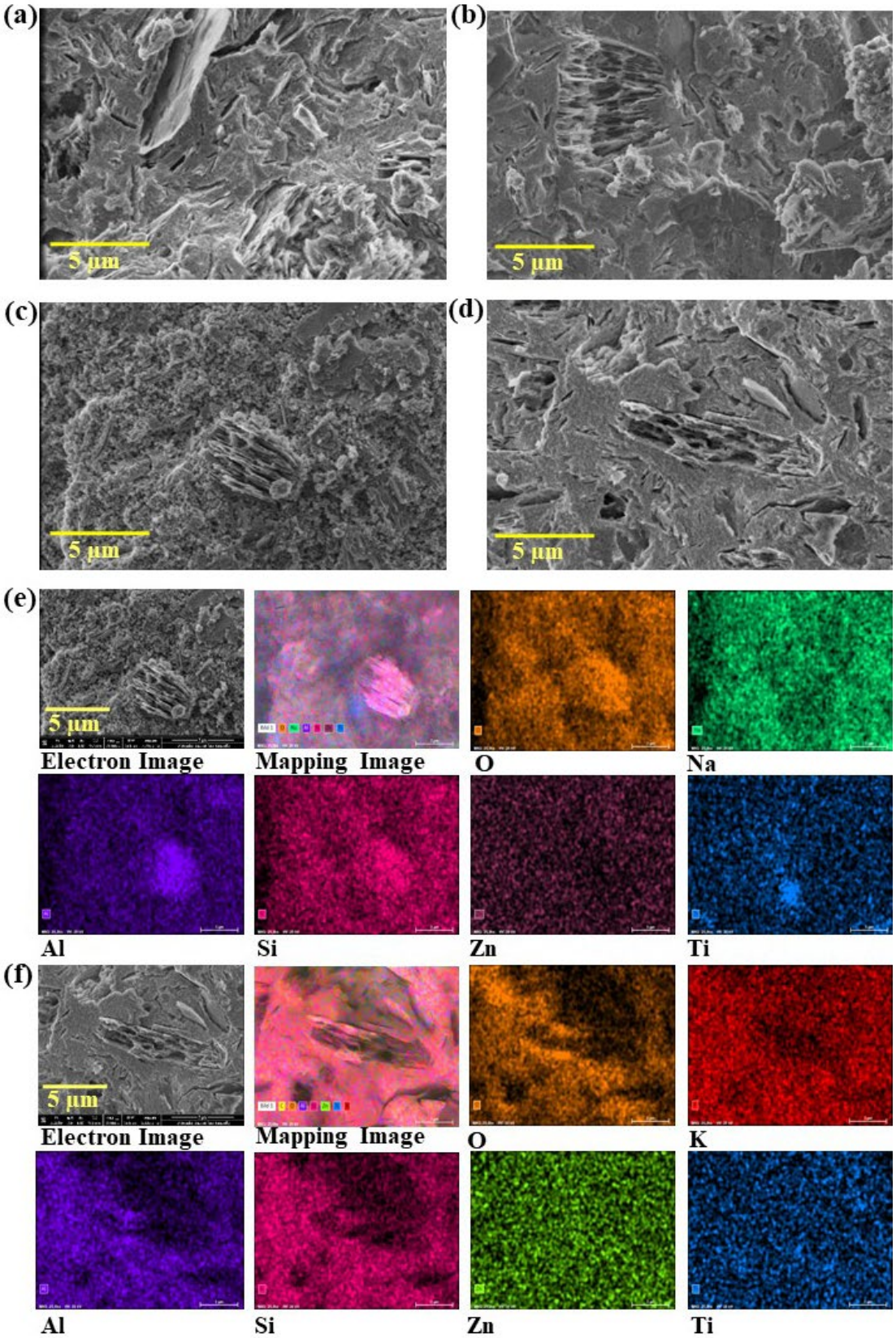


**Figure 7.** SEM image with elemental mapping of 28-d cured geopolymer pastes: (a) SEM image of S/N 1.0; (b) SEM image of S/K 1.0; (c) SEM image of S/N 1.0-Z; (d) SEM image of S/K 1.0-Z; (e) element mapping of S/N 1.0-Z; (f) element mapping of S/K 1.0-Z.

### *3.3 Effects of Zn and Zn-rich Sludge on Physicochemical Properties of Geopolymer*

Figure 8a shows the setting time for the geopolymer pastes with and without ZnO. High-alkali S/N 0.5 samples yielded the shortest initial setting time of 3.1 h and final setting time of 4.1 h. The setting times increased along with the increase of Si/Na molar ratio, because Si and Al cations dissolving in low-alkali samples gradually reached their critical limits of nucleation and growth of the geopolymer gel. By comparison, K-activated geopolymer systems showed the same trend, with the initial and final setting times being relatively long compared to samples where Na is the alkali source, consistent with isothermal calorimetry results (Figure 1). The substitution of ZnO (Al/Zn molar ratio of 4) significantly delayed both the initial and final setting times in Na-activated geopolymer systems, especially for low-alkali samples. Zn also had an inhibitory effect on the K-activated geopolymer systems; however, its magnitude was relatively small in comparison with Na-activated geopolymer systems, consistent with isothermal calorimetry results. The addition of additional ZnO in geopolymer systems also caused a dramatic delay of initial and final setting times (Figure S5), likely due to the formation of metastable Na/K-Zn phase as discussed in Section 3.1. This excludes the possibility of the delayed setting time resulting from lower Al/Si content. Note that the addition of high-dosage Zn would completely poison the reaction of PC and Ca-rich alkali-activated materials [36,47], whereas Zn only retarded the reaction process of N/K-based geopolymer systems. This indicates that N/K-activated geopolymers exhibit favourable compatibility with Zn during the early stage of reaction, and K-activated geopolymer systems show greater compatibility with Zn than Na-activated geopolymer systems.

Figure 8b illustrates the TCLP leaching concentrations of Zn and the corresponding pH values of leachate from 28-d cured Zn-incorporated geopolymer samples. The S/N 0.5-Z samples showed the lowest Zn leachability (1.4 mg $L^{-1}$), indicating strong incorporation of Zn in the

413 geopolymer gel. The Zn leachability significantly increased with increased of Si/Na molar ratio
414 (i.e. decreased alkali content). Interestingly, the Zn leachability of S/K 0.5-Z samples (106.6
415 mg $L^{-1}$) was 75 times higher than that of S/N 0.5-Z samples. This is likely due to the differences
416 in ionic radii of $Na^+$ (116 pm) and $K^+$ (152 pm), with $Zn^{2+}$ (ionic radius of 88 pm) more easily
417 substituted for $Na^+$ than $K^+$. This is consistent with the findings from $^{29}Si$ MAS NMR data
418 (Figure 4) discussed above. The relatively dense structure of S/N 1.0-Z sample (Figure S4)
419 may also be favourable for the Zn immobilisation. Additionally, the lower pH value exhibited
420 by the solution for S/K 0.5-Z samples (~7.5) compared with S/N 0.5-Z samples (~8.5) will also
421 contribute to the higher leachability of Zn from S/K 0.5-Z samples, due to the greater solubility
422 of $Zn^{2+}$ at lower pH [48]. The TCLP results demonstrate that Na-activated geopolymer cements
423 exhibit excellent immobilisation of Zn, with the use of high-alkali activators enhancing the
424 effectiveness of S/S.

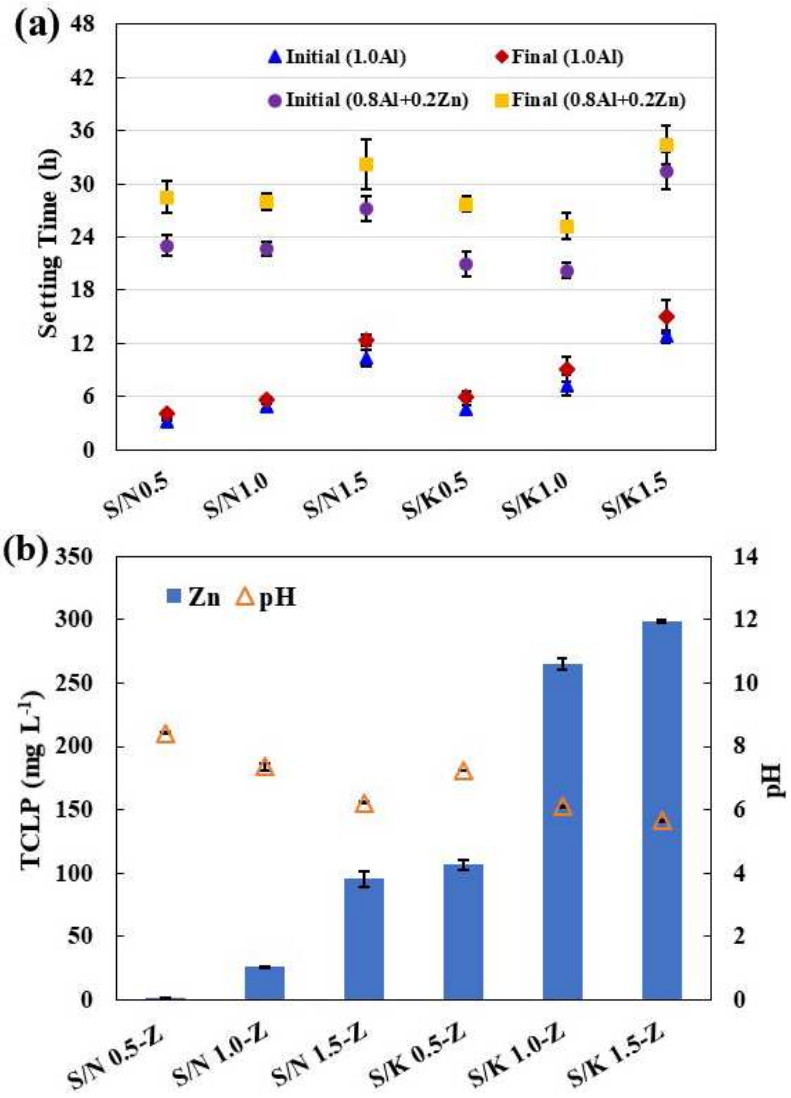


**Figure 8.** Setting time and leachability of geopolymer pastes cured for 28 days: (a) setting time of geopolymer pastes with or without ZnO (20 mol.%) replacement; (b) Zn concentration and pH in leachate from ZnO-incorporated geopolymer pastes.

The effects of Zn-rich electroplating sludge on the physicochemical properties of geopolymer were evaluated in terms of setting time, TCLP leachability, and compressive strength. As shown in Figure 9a, the addition of 50% sludge (N-S1 sample) postponed the final setting time from 5.6 h to 23.4 h. The setting time was prolonged with increasing dosages of sludge. Although the final setting time of N-S4 samples reached 39.3 h, the setting and hardening process still occurred in approximately 80% sludge-incorporated samples. Zn-rich sludge addition showed a relatively small inhibitory effect on the K-activated geopolymer when

compared to Na-activated geopolymer samples, consistent with the effect of pure ZnO (Figure 9a).

From Figure 9b, the TCLP leachate for electroplating sludge contained 516.7 mg $L^{-1}$ of Zn, 77.7 mg $L^{-1}$ of Ni, 77.5 mg $L^{-1}$ of Mn and 11.2 mg $L^{-1}$ of Co. The Zn leachability exceeded the TCLP limit (250 mg $L^{-1}$) of landfill disposal criteria [49]. After the S/S process, the respective leachability of the various toxic elements from N-S1 samples (with 50% sludge) was reduced by 95.4% to 98.7%. However, Zn leachability dramatically increased to 285.5 mg $L^{-1}$ when the mass ratio of sludge/Na-geopolymer was 2. This indicated that high sludge dosages (66.6 wt%) exceeded the critical point required for a stable (Na,Zn)-A-S-H gel and resulted in extremely high Zn leachability. Note that the leachability of other potentially toxic elements also increased with the increase in sludge dosage. Similar performance results imply that these divalent cations ($Mn^{2+}$, $Co^{2+}$, $Ni^{2+}$) also might substitute monovalent charge $Na^{+}$ cation in charge balancing sites in the geopolymer gel. The Zn leachability of the K-S1 sample was 7.1 times higher than the value of N-S1 sample, consistent with the effect of pure ZnO (Figure 7a). From Figure S6, after 28-d curing, all the sludge-incorporated samples solidified with at least some degree of compressive strength (> 0.15 MPa). There was a negative correlation between compressive strength and leachability. These data show that Na-activated geopolymers are excellent candidates for the S/S of Zn-rich electroplating sludge. For practical S/S application, the dosage of sludge should be well controlled to avoid exceeding the critical point required for a stable (Na,Zn)-A-S-H gel.

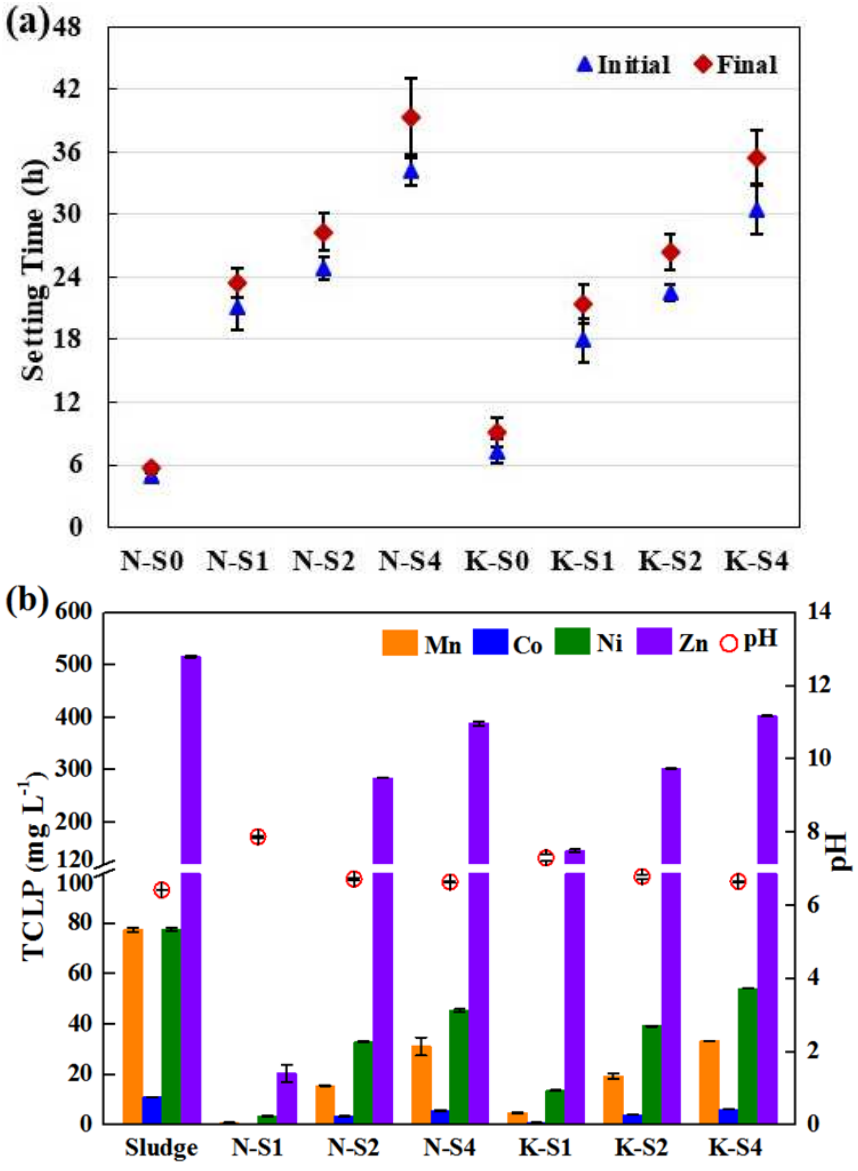


**Figure 9.** Setting time and leachability of geopolymer with various amounts of industrial sludge ($SiO_2/M_2O$ molar ratio of 1.0): (a) setting time of sludge-added geopolymer samples; (b) element concentrations and pH in leachate from sludge-added geopolymer samples. (N/K-Sx: sodium/potassium silicate-activated geopolymer/sludge mass ratio of 1/x).

## 4. Conclusions

This study investigated the role of Zn on the reaction kinetics, phase assemblage and nanostructure of metakaolin-based geopolymer cements, and evaluated the feasibility of using metakaolin-based geopolymer cements for the S/S treatment of Zn-rich industrial sludge. Experimental results showed that ZnO substitution significantly inhibited the alkali-activation reaction and prolonged setting time, especially for low-alkali geopolymers, probably due to the

formation of metastable "Na/K-Zn" phase materials. ZnO substitution had a slight inhibitory effect on the alkali-activation reaction in K-activated geopolymer systems compared to Na-activated geopolymer systems. XRD results showed that upon alkali-activation ZnO reacted completely after 7 days curing, and formed amorphous products; however, ZnO did not significantly change the nanostructure of the primary reaction product ((N,K)-A-S-H gel), as evidenced by $^{27}$Al MAS NMR results. $^{29}$Si MAS NMR spectra illustrated that after substitution of ZnO, the content of $Q^4$(4Al) sites increased while $Q^4$(3Al) decreased, resulting in a decrease of Si/Al ratio in the (N,K)-A-S-H gel. This indicated that $Zn^{2+}$ partially substituted for $Na^+/K^+$ cations in charge balancing sites within the (Na,K)-A-S-H gel. This partial substitution of $Zn^{2+}$ for $Na^+/K^+$ occurred to a greater extent in Na-activated geopolymer gel than in K-activated geopolymer gel, which might be due to discrepancy in the ionic radii of $Na^+$ and $K^+$. As a result, the TCLP leachability of Zn from Na-activated samples was relatively low. The S/S experiments verified that K-activated geopolymer reaction kinetics were less inhibited by addition of Zn-rich sludge, however Na-activated geopolymer samples exhibited greater immobilisation capacity for Zn. In practical applications, alkali dosage, sludge content, and other conditions should be optimised to achieve excellent and robust S/S performance. Together, these findings reveal the reaction inhibiting and incorporation mechanisms of Zn in geopolymer systems and suggest a sustainable and efficient geopolymer binder for S/S of Zn-rich sludge.

**Acknowledgements**

The authors gratefully acknowledge the financial support from the Hong Kong Research Grants Council (PolyU 15223517) and the Alexander von Humboldt Foundation (AvH) for this study. The authors appreciate the support of the University Research Facility on Chemical and Environmental Analysis (URFCE) of PolyU, and the experimental assistance from Dr Oday

Hussein (University of Sheffield), Mr Liang Chen (PolyU), and Ms Simone Hempel (TU Dresden) in this study. The authors also thank the PQ Corporation for the provision of alkali silicate solutions for this study.

## References

[1] J.L. Provis, Alkali-activated materials, Cem. Concr. Res. 114 (2018) 40-48.

[2] J.L. Provis, S.A. Bernal, Geopolymers and related alkali-activated materials, Annu. Rev. Mater. Res. 44 (2014) 299-327,

[3] C. Shi, B. Qu, J.L. Provis, Recent progress in low-carbon binders, Cem. Concr. Res. 122 (2019) 227-250.

[4] Y.H.M. Amran, R. Alyousef, H. Alabduljabbar, M. El-Zeadani, Clean production and properties of geopolymer concrete; A review, J. Clean. Prod. 251 (2020) 119679.

[5] J.L. Provis, A. Palomo, C. Shi, Advances in understanding alkali-activated materials, Cem. Concr. Res. 78 (2015) 110-125.

[6] M. Lahoti, K.H. Tan, E.H. Yang, A critical review of geopolymer properties for structural fire-resistance applications, Constr. Build. Mater. 221 (2019) 514-526.

[7] M. Vafaei, A. Allahverdi, P. Dong, N. Bassim, Acid attack on geopolymer cement mortar based on waste-glass powder and calcium aluminate cement at mild concentration, Constr. Build. Mater. 193 (2018) 363-372.

[8] D.A. Geddes, X. Ke, S.A. Bernal, M. Hayes, J.L. Provis, Metakaolin-based geopolymers for nuclear waste encapsulation. Calcined Clays Sustain. Concr. (2018) 183-188.

[9] Q. Tian, K. Sasaki, A novel composite of layered double hydroxide/geopolymer for co-immobilization of $Cs^{+}$ and $SeO_4^{2-}$ from aqueous solution, Sci. Total Environ. 695 (2019) 133799.

[10] V.A. Reddy, C.H. Solanki, S. Kumar, K.R. Reddy, Y.J. Du, New ternary blend limestone calcined clay cement for solidification/stabilization of zinc contaminated soil, Chemosphere 235 (2019) 308-315.

[11] L. Wang, L. Chen, D.C.W. Tsang, Y.Y. Zhou, J. Rinklebe, H. Song, E.E. Kown, K. Baek, Y.S. Ok, Mechanistic insights into red mud, blast furnace slag, or metakaolin-assisted stabilization/solidification of arsenic-contaminated sediment, Environ. Int. 133 (2020) 105247.

[12] L. Wang, D.W. Cho, D.C.W. Tsang, X.D. Cao, D.Y. Hou, Z.T. Shen, D.S. Alessi, Y.S. OK, C.S., Poon, Green remediation of As and Pb contaminated soil using cement-free clay-based stabilization/solidification, Environ. Int. 126 (2019) 336-345.

[13] L. Wang, L. Chen, D.W. Cho, D.C.W. Tsang, J. Yang, D.Y. Hou, K. Baek, H.W. Kua, C.S. Poon, Novel synergy of Si-rich minerals and reactive MgO for stabilization/solidification of contaminated sediment, J. Hazard Mater. 365 (2019) 695-706.

[14] S.S.G. Hashemi, H.B. Mahmud, T.C. Ghuan, A.B. Chin, C. Kuenzel, N. Ranjbar, Safe disposal of coal bottom ash by solidification and stabilization techniques, Constr. Build. Mater. 197 (2019) 705-715.

[15] L. Wang, L. Chen, B. Guo, D.C.W. Tsang, L, Huang, Y.S. Ok, V. Mechtcherine, Red mud-enhanced magnesium phosphate cement for remediation of Pb and As contaminated soil, J. Hazard Mater. 400 (2020) 123317.

[16] Q.Y. Chen, M. Tyrer, C.D. Hills, X.M. Yang, P. Carey, Immobilisation of heavy metal in cement-based solidification/stabilisation: A review, Waste Manage. 29 (2009) 390-403.

[17] L. Wang, K.Q. Yu, J. Li, D.C.W. Tsang, C.S. Poon, J.C. Yoo, K. Baek, S.M. Ding, D.Y. Hou, J.G. Dai, Low-carbon and low-alkalinity stabilization/solidification of high-Pb contaminated soil. Chem. Eng. J. 351 (2018) 418-427.

547 [18] J. Liu, H. Jin, C. Gu, Y. Yang, Effects of zinc oxide nanoparticles on early-age hydration
548 and the mechanical properties of cement paste, Constr. Build. Mater. 217 (2019) 352–362.
549 [19] N. Gineys, G. Aouad, D. Damidot, Managing trace elements in Portland cement – Part II:
550 Comparison of two methods to incorporate Zn in a cement, Cement Concrete Comp. 33
551 (2011) 629–636.
552 [20] N. Gineys, G. Aouad, F. Sorrentino, D. Damidot, Incorporation of trace elements in
553 Portland cement clinker: Thresholds limits for Cu, Ni, Sn or Zn, Cement Concrete Res. 41
554 (2011) 1177–1184.
555 [21] K. Zhang, F. Wang, M. Rao, W. Zhang, X. Huang, Influence of ZnO-doping on the
556 properties of high-ferrite cement clinker, Constr. Build. Mater. 224 (2019) 551–559.
557 [22] N. Garg, C.E. White, Mechanism of zinc oxide retardation in alkali-activated materials:
558 an in situ X-ray pair distribution function investigation, J. Mater. Chem. A, 5 (2017) 11794.
559 [23] F.F. Ataie, M.C.G. Juenger, S.C. Taylor-Lange, K.A. Riding, Comparison of the retarding
560 mechanisms of zinc oxide and sucrose on cement hydration and interactions with
561 supplementary cementitious materials, Cement Concrete Res. 72 (2015) 128–136.
562 [24] N. Tripathi, G. Choppala, R.S. Singh, Evaluation of modified chitosan for remediation of
563 zinc contaminated soils, J. Geochem. Explor. 182 (2017) 180-184.
564 [25] M. Yoldi, E.G. Fuentes-Ordoñez, S.A. Korili, A. Gil, Zeolite synthesis from industrial
565 wastes, Micropor. Mesopor. Mat. 287 (2019) 183-191.
566 [26] J.M. Moreno-Maroto, P.N. Camacho, T. Cotes-Palomino, C.M. García, J. Alonso-
567 Azcárate, Manufacturing of lightweight aggregates from biomass fly ash, beer bagasse,
568 Zn-rich industrial sludge and clay by slow firing. J. Environ. Manage. 246 (2019) 785-795.
569 [27] S.A. Bernal, E.D. Rodríguez, A.P. Kirchheim, J.L. Provis, Management and valorisation
570 of wastes through use in producing alkali-activated cement materials, J. Chem. Technol.
571 Biot. 91 (2016) 2365-2388.

572 [28] B. Walkley, X. Ke, O.H. Hussein, S.A. Bernal, J.L.Provis, Incorporation of strontium and
573 calcium in geopolymer gels, J. Hazard Mater. 382 (2020) 121015.
574 [29] F. Demoisson, R. Piolet, F. Bernard, Hydrothermal synthesis of ZnO crystals from
575 $Zn(OH)_2$ metastable phases at room to supercritical conditions. Cryst. Growth Des. 14
576 (2014) 5388−5396.
577 [30] BS EN 480-2, Admixtures for concrete, mortar and grout Test methods Part 2:
578 Determination of setting time, British Standards Institution, London, UK (2006).
579 [31] BS EN 12390, Testing hardened concrete compressive strength of test specimens, British
580 Standards Institution, London, UK (2009).
581 [32] US EPA 1311. Toxicity characteristic leaching procedure, U.S. Environmental Protection
582 Agency, Washington DC, USA (1992).
583 [33] J.L. Provis, P. Duxson, G.C. Lukey, J.S.J. van Deventer, Statistical thermodynamic model
584 for Si/Al ordering in amorphous aluminosilicates, Chem. Mater 17 (2005) 2976-2986.
585 [34] G. Engelhardt, U. Lohse, E. Lippmaa, M. Tarmak, M. Mägi, $^{29}$Si-NMR untersuchungen
586 zur verteilung der silicium-und aluminiumatome im alumosilicatgitter von zeolithen mit
587 faujasit-struktur, Z. Anorg. Allg. Chemie. 482 (1981) 49–64.
588 [35] C.E. Tommaseo, M. Kersten, Aqueous solubility diagrams for cementitious waste
589 stabilization systems. 3. mechanism of zinc immobilizaton by calcium silicate hydrate,
590 Environ. Sci. Technol. 36 (2002) 2919–2925.
591 [36] G. Liang, H. Zhu, Z. Zhang, Q. Wu, Effect of rice husk ash addition on the compressive
592 strength and thermal stability of metakaolin based geopolymer, Constr. Build. Mater. 222
593 (2019) 872-881.
594 [37] P. Raphaëlle, C. Martin, B. Raphaël, Influence of the initial water content in flash calcined
595 metakaolin-based geopolymer, Constr. Build. Mater. 201 (2019) 421-429.

596 [38] A. Hosan, S. Haque, F. Shaikh, Compressive behaviour of sodium and potassium
597 activators synthetized fly ash geopolymer at elevated temperatures: a comparative study.
598 J. Build. Eng. 8, (2016) 123-130.
599 [39] T.S. Rocha, D.P. Dias, F.C.C. França, R.R.S. Guerra, L.R.C.O. Marques, Metakaolin-
600 based geopolymer mortars with different alkaline activators ($Na^+$ and $K^+$), Constr. Build.
601 Mater. 178 (2018) 453–461.
602 [40] S.V. Nistor, D. Ghica, M. Stefan, I. Vlaicu, J.N. Baarascu, C. Bartha, Magnetic defects in
603 crystalline $Zn(OH)_2$ and nanocrystalline ZnO resulting from its thermal decomposition, J.
604 Alloy. Comp. 548 (2013) 222-227.
605 [41] D.H. Piva, R.H. Piva, M.C. Rocha, J.A. Dias, I. Malavazi, M.R. Morelli, Antibacterial and
606 photocatalytic activity of ZnO nanoparticles from $Zn(OH)_2$ dehydrated by azeotropic
607 distillation, freeze drying, and ethanol washing, Adv. Powder Technol. 28, (2017) 463-
608 472.
609 [42] M.R. Anseau, J.P. Leung, N. Sahai, T.W. Swaddle, Interactions of silicate ions with
610 zinc(II) and aluminum(III) in alkaline aqueous solution, Inorg. Chem. 44 (2005) 8023-
611 8032.
612 [43] B. Walkley, J.L. Provis, Solid-state nuclear magnetic resonance spectroscopy of cements,
613 Mater. Today Adv. 1 (2019) 100007.
614 [44] R.D. Shannon, Revised effective ionic radii and systematic studies of interatomic distances
615 in halides and chalcogenides, Acta. Crystallogr. A. 32 (1976) 751–767.
616 [45] B. Walkley, G.J. Rees, R.S. Nicolas, J.S.J. van Deventer, J.V. Hanna, J.L. Provis, New
617 structural model of hydrous sodium aluminosilicate gels and the role of charge-balancing
618 extra-framework Al, J. Phys. Chem. C. 122 (2018) 5673–5685.

[46] J.F. Stebbins, S. Kroeker, S.K. Lee, T.J, Kiczenski, Quantification of five- and six-coordinated aluminum ions in aluminosilicate and fluoride-containing glasses by high-field, high-resolution $^{27}$Al NMR, J. Non-Cryst. Solids 275 (2000) 1–6.

[47] K.G. Kolovos, S.B. Glikeria, K. Glikeria, K.S. Tsivilis, CuO and ZnO addition in the cement raw mix: Effect on clinkering process and cement hydration and properties, Ceramic-Silikaty 49 (2005) 205-212.

[48] R.A. Reichle, K.G. Mccurdy, L.G. Hepler, Zinc hydroxide: solubility product and hydroxy-complex stability constants from 12.5-75 °C, Can. J. Chem. 53 (1975) 3841-3845.

[49] HK EPD, Practice guide for investigation and remediation of contaminated land, Environmental protection department, Hong Kong (2011).